Entrance channel limit on the fusion of ^{28}Si with ^{12}C at high energy

B. A. Harmon
Department of Physics, University of Virginia, Charlottesville, Virginia 22901
and Oak Ridge National Laboratory, Oak Ridge, Tennessee 37831

S. T. Thornton
Department of Physics, University of Virginia, Charlottesville, Virginia 22901

D. Shapira and J. Gomez del Campo
Oak Ridge National Laboratory, Oak Ridge, Tennessee 37831

M. Beckerman
Joint Institute for Heavy Ion Research, Oak Ridge, Tennessee 37831
and Oak Ridge National Laboratory, Oak Ridge, Tennessee 37831
(Received 24 February 1986)

Cross sections for the fusion of $^{28}Si+^{12}C$ have been measured at center of mass bombarding energies of 39, 43.5, 48, and 54 MeV. Velocity and energy spectra of reaction products having charge $Z \geq 12$ and mass number $A \geq 24$ were studied at several angles between $\theta_{lab}=2°$ and 13°. Separation of fusion from other processes was made by comparison of kinematic calculations to measured spectra. The extracted critical angular momentum (l_{cr}^{fus}) of $22\hbar$ indicates the existence of an entrance-channel-imposed limit on the high energy fusion cross section. More symmetric systems forming the same compound nucleus, ^{40}Ca, have considerably larger limiting angular momenta. This result is consistent with the previous observation of a maximum angular momentum of $22\hbar$ (relative to the entrance channel) for the orbiting dinuclear complex found in studies of back-angle deeply inelastic scattering of ^{28}Si and ^{12}C.

I. INTRODUCTION

The fusion of heavy ions in light systems (mass numbers $A_{proj}+A_{targ} \leq 40$) has been studied extensively at energies above the classical Coulomb barrier.[1-6] Much of the effort towards understanding the behavior of the fusion cross section (σ_{fus}) has been to determine how σ_{fus} is influenced by (1) the entrance channel projectile and target characteristics, or (2) the availability of states in the compound nucleus. Evidence exists that either of these effects can "define" or "limit" the magnitude of σ_{fus} through the angular momentum the system is able to support. For a given energy, it is still not clear from the available data which of the two mechanisms will determine the magnitude of the fusion cross section.

Figure 1 shows some general features of the fusion cross section in light-heavy ion systems which have emerged in the data of many experiments.[1-6] The dependence of σ_{fus} on bombarding energy can be characterized by three regions. At bombarding energies not far above the Coulomb barrier (region I), it has been shown that the entrance channel nucleus-nucleus potential determines whether the nuclei fuse.[7,8] A repulsive barrier exists in the potential due to a superposition of the potential's nuclear, Coulomb, and centrifugal components. As long as the projectile energy is sufficient to overcome the barrier, fusion will occur, and in fact, dominates all other nonelastic processes. Consequently, the magnitude of the fusion cross section in region I is nearly equal to the total reaction cross section (σ_{reac}). The height of the barrier obtained from low energy fusion data is observed to be a smooth function of the radii of the entrance channel nuclei, and phenomenological fusion models have incorporated this finding successfully.[8-13]

The picture is more uncertain for fusion at intermediate and high energies (regions II and III in Fig. 1, respectively). In region II the fusion cross section may show a

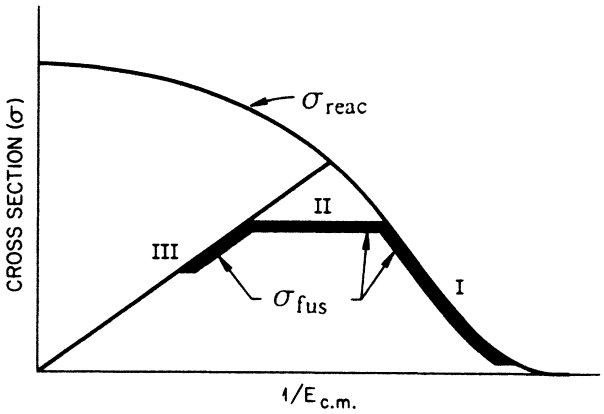

FIG. 1. The general behavior of the fusion (σ_{fus}) and total reaction cross sections (σ_{reac}) as a function of the reciprocal of the center of mass bombarding energy. Regions I–III indicate energy regimes of σ_{fus} discussed in the text.

slight increase with bombarding energy, but falls short of the total reaction cross section. Still higher in bombarding energy, σ_{fus} has been observed to decrease linearly as the inverse of the incident beam energy (region III). A number of models that account for the behavior of σ_{fus} have been put forth; generally, these models have approached fusion from the point of view that the fusion cross section is either limited by the properties of the compound nucleus[4,9–11] or the entrance channel.[12–14]

The compound nucleus-imposed limitation models postulate that, although the nuclei are in contact and able to interact, the lack of available states in energy–angular momentum space prevents the compound nucleus from forming. These models differ in the manner in which that condition is realized. In some instances the relative orbital angular momentum brought in by the colliding nuclei is so high that the resulting compound nucleus becomes unstable against fission. This dictates an upper limit for the partial waves that can fuse and accounts for the observed decrease in the fusion cross section in region III.[6] According to these same models, the limit on fusion in region II is also due to the high angular momenta populated in such collisions. For a compound nucleus to form, a certain minimum density of high spin levels is required at the appropriate excitation energy. The required level densities at each excitation energy produce a locus of points in the energy versus angular momentum plane (E-J plane). The fusion of light nuclei at a given bombarding energy is limited by this "shifted" yrast line.[10] In a different approach, an alternate locus in the E-J plane is dictated by requiring sufficient level overlap in the compound nucleus that is to be formed.[11]

In the entrance channel models the ability of the nuclei to capture one another is the main factor limiting the fusion. It is only required that the nuclei overcome their mutual Coulomb and centrifugal repulsion and approach to a certain critical distance for fusion to take place.[8] Other models[13,14] include the effects of contact friction between the nuclei. These entrance channel models,[13,14] which incorporate the effects of conservative and dissipative forces, can reproduce the observed behavior of the fusion cross section over the entire energy range (regions I–III).

All the models mentioned above suffer from the lack of a precise knowledge of physical quantities needed as input to model calculations such as the nucleus-nucleus potential, the level density, or the yrast line for high excitation energies. It is the measured fusion cross sections themselves that constrain these parameters. The smooth and systematic behavior of such parameters that was derived from studies of fusion cross sections at low energies did not materialize in the studies at higher energies (regions II and III). These problems are due in large part to the difficulty of measuring precise fusion data at these higher energies in the presence of many other competing processes. Such processes, on the other hand, could provide a means of obtaining information about the physical quantities used in the fusion models. A method of constraining the parameters of a model calculation could be quite valuable where extensive fusion data have not yielded reliable systematics.

In prior studies of collisions between ^{12}C and ^{28}Si,[15,16] large yields from deeply inelastic reactions were discovered at backward angles. These yields have the characteristics of the decay products of an orbiting dinuclear complex formed in the collision. An analysis of the kinetic energy of these products showed that the kinetic energy equaled the sum of nuclear, Coulomb, and centrifugal energies stored in the rotating dinuclear complex. The observation of a saturation in the total kinetic energies at high bombarding energy was interpreted as evidence that a maximum angular momentum the orbiting system could sustain without being overwhelmed by centrifugal repulsion had been surpassed. Some of the entrance channel models for fusion[13,14] also use the nucleus-nucleus potential and one body dissipation to determine conditions for fusion. The potential parameters derived from the analysis of the orbiting data can now be used in these models to predict the fusion cross sections.

In this paper we report on a study of the fusion of ^{28}Si and ^{12}C in the energy range 4.6–6.4 MeV/nucleon to search for the limiting angular momentum of the system at high energy (region III). In Sec. II we describe how the experiment was designed in order to measure fusion cross sections at high energy. Following this, in Sec. III, is a discussion of the method used to separate compound nucleus evaporation residues from other nonelastic yields. In Secs. IV and V we discuss the connection between fusion and orbiting processes, and conclude with possible routes for further investigation.

II. EXPERIMENTAL PROCEDURE

We have planned to use the kinematic properties of reaction products in the ^{28}Si + ^{12}C system to help us discriminate between the yields that originate from nonelastic processes and those from fusion. It was necessary, therefore, to determine the mass and charge of each detected particle and to obtain velocity spectra for individual isotopes. The kinetic energy, specific energy loss, and time of flight (TOF) over a fixed distance were measured for all products with atomic numbers (Z) ranging from 12 to 20. Using the heavier ^{28}Si nucleus as the projectile to bombard ^{12}C targets produces a compound nucleus with sufficient kinetic energy to provide the timing signal, energy loss, and full energy signal with minimal straggling and low energy cutoff problems.

Heavy products ($Z \geq 12$, $A \geq 24$) were identified by the experimental apparatus shown in Fig. 2. The setup consisted of a small target chamber, to which a movable time-of-flight arm was attached. The TOF arm structure supports rigid mounts for both timing and energy detectors and a separate vacuum system from the scattering chamber. Solid state monitor detectors (LM and RM) were placed in the scattering chamber at fixed angles with respect to the beam axis. A small aperture is used at the entrance to the TOF arm near the scattering chamber wall to reduce the count rate due to elastics at the very forward angles.

Beams of 130, 145, 160, and 180 MeV ^{28}Si (4.6–6.4 MeV/nucleon) from the Brookhaven National Laboratory tandem facility and 180 MeV at the Oak Ridge National

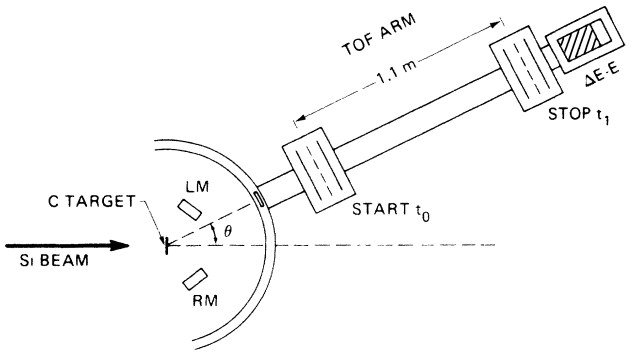

TOF ARM ($\Delta\Omega$ = 0.0338 msr)

SIGNAL	DETECTOR	RESOLUTION (130 MeV)
ΔE	IONIZATION CHAMBER	0.87 MeV FWHM (5.9%)
E	SOLID STATE COUNTER	1.7 MeV FWHM (1.4%)
TOF = $t_1 - t_0$	PPAC/MWPC HYBRID	360 ps FWHM (1.0%)

FIG. 2. The experimental apparatus and signal resolutions for 130 MeV ^{28}Si on ^{12}C.

Laboratory Holifield Heavy Ion Research Facility (HHIRF) tandem were used to bombard carbon foils of thicknesses 20 and 100 μg/cm^2. The grazing angle for ^{28}Si scattering from ^{12}C at the bombarding energies used is very small ($\theta_{gr} \leq 8°$). For this reason, the targets were coated with a thin layer of evaporated gold (less than 2 μg/cm^2) for normalization of the measured cross sections to Rutherford scattering of ^{28}Si from ^{197}Au.

A number of different types of detectors were used in this experiment; however, the method which was used to extract charge and mass information was always the same. Two timing detectors provide the time of flight which yields both the velocity of the reaction product, and when combined with the energy, the mass of the product. Charge identification was provided by comparing specific energy loss to the total energy deposited when the reaction product is stopped in an ionizing medium. At the Brookhaven Laboratory, two Breskin-type parallel plate avalanche counter/multiwire proportional counter hybrids[17] (PPAC/MWPC) were used to measure time of flight. One detector provided a start signal for the time to amplitude converter and the other provided a stop. An ionization chamber used to measure energy loss (ΔE) and a solid state (500 μm thick) detector used to measure the energy of the reaction products were mounted behind the timing detectors. Gas pressures were 2–3 Torr and 28–29 Torr (isobutane) for the timing and ΔE detectors, respectively. Typical detector resolutions [full width at half maximum (FWHM)] at $E_{lab} = 130$ MeV are shown in the table accompanying Fig. 2. For all beam energies, the energy resolution was $\leq 1.2\%$ (FWHM) and the timing resolution was 1.0% (FWHM), yielding a typical overall mass resolution of $\leq 3.2\%$. The best mass resolution, 2.8%, was obtained at 180 MeV. The experiment at HHIRF was performed with a somewhat better system in terms of timing resolution. In this case, the gas detector closest to the scattering chamber was replaced by a microchannel plate/carbon foil assembly. In place of the ΔE-E gas/solid state detector, we used a deep (1 m) gas ionization chamber[18] that records energy loss across four electrodes of varying lengths as the particle is stopped in the gas volume. This system provides better timing resolution (see Fig. 3, $\Delta t = 220$ ps) and accommodates the extreme energy range of compound nucleus evaporation residues. Initially the stop detector at HHIRF was a PPAC, but was upgraded to a position-sensitive PPAC/MWPC that provides the capability for monitoring the profile of the scattered particles entering the rear section of the time-of-flight arm.

Measurements were made for several angles between $\theta_{lab} = 2°–13°$ at 130 and 180 MeV, and for $\theta_{lab} = 3°$ at 145 and 160 MeV. For $\theta_{lab} < 4°$, the solid angle spanned by the TOF arm was reduced from 0.135 to 0.034 msr by changing the diameter of the TOF entrance aperture. A measurement of the elastic cross section was made at $\pm 3°$ to determine the 0° position with respect to the beam. Rutherford scattering of a 50 MeV ^{28}Si beam was used for energy and velocity calibration of the detection system as well as for determination of the relative amounts of Au and C atoms in the target foil. The uncertainty in the determination of the cross section associated with the experimental procedure includes uncertainties in the left-right symmetry with respect to the beam axis (3.5%), determination of the monitor angle ($\approx 3.4\%$), and solid angle spanned by TOF arm and monitors ($\approx 10\%$). These uncertainties combine for an overall uncertainty of 11%.

III. ANALYSIS OF ENERGY AND VELOCITY SPECTRA

We have performed a kinematic analysis of the data at all beam energies in order to separate compound nucleus evaporation residues from other heavy reaction products. Extensive use has been made of statistical evaporation codes for the simulation of kinematic features resulting from the deexcitation of ^{40}Ca* by successive emission of light particles ($A \leq 4$). Other kinematic simulations have been helpful in instances where some portions of the data do not appear to result from evaporative decay of the compound nucleus, and these are described below.

Figure 3 is a two-dimensional map of deposited energy (E) versus the product of deposited energy and the square of the time of flight (Et^2) for all reaction products at $E_{lab} = 180$ MeV, $\theta_{lab} = 5°$. The horizontal axis (Et^2) is proportional to the detected mass. A range of masses with A (mass number) from 24 to 37 are indicated by arrows. No gating has been carried out in Fig. 3, so each mass (line) contains a number of differently charged reaction products. Once a gate has been drawn on a single charge (identified using energy and energy loss information from the gas counter), a mass spectrum for reaction products of the same charge will contain, on average, two to four mass lines.

A significant problem relevant to Fig. 3 exists in a system where time of flight and energy are recorded for the same particle. There is always the unwanted loss in energy of the reaction products as they pass through the two timing detectors before reaching the ionization chamber.

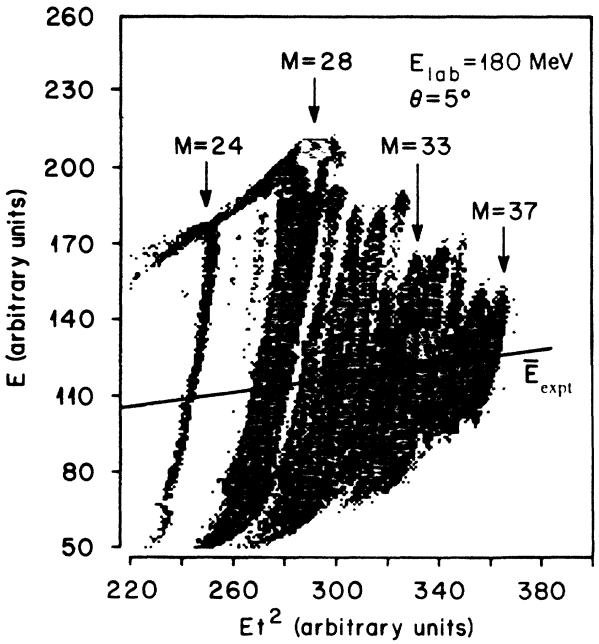

FIG. 3. Two dimensional plot of total energy vs energy times time of flight squared for ^{28}Si + ^{12}C at $E_{lab}=180$ MeV, $\theta_{lab}=5°$. Masses from $A=24$ to 37 are visible. The line across the figure indicates the location of the most probable energy of the compound nucleus residue.

The mass spectrum of Fig. 3 is an optimum case in which the apparatus consisted of a microchannel plate detector and the thinnest (three foils) parallel plate avalanche counter that was available to us. Therefore it is possible to visually separate the mass lines in the on-line spectrum of Fig. 3. However, in the experiment with two gas timing detectors (as represented schematically in Fig. 2), the number of foils the particles were required to pass through were significantly larger (four additional thin foils), and corrections for energy loss were necessary before mass gates could be drawn. The overall increase in the width of the mass lines with respect to the vertical axis as the mass number decreases is due to the increasing number of evaporated particles from the compound nucleus as we move farther from $A=40$.

The elastic scattering peaks were used to calibrate the energy and velocity spectra. The velocity calibration yields centroids of the experimental velocity distributions $\bar{v}$ for evaporation residues within 1.0% of the predicted values,[19] $\bar{v}=v_{CN}\cos\theta_{lab}$ at 180 MeV and 2.9% at 130 MeV. The energy calibration was performed after correction for losses through gas and foils. The predicted centroids $\bar{E}\approx M_R E_{CN}/M_{CN}\cos^2\theta_{lab}$ were in agreement with the $\bar{E}_{expt}$ for masses near that of the beam ($A=29$–33), but for lighter masses the centroids became increasingly less than $\bar{E}$ such that $(\bar{E}_{expt}-\bar{E})/\bar{E}\sim 7\%$ for $A=37$. We attribute this discrepancy to the energy loss correction procedure, where energy loss tables[20] and semiempirical formulae were used to estimate the energy loss in the different foils and gas volumes.

If light particle emission is assumed to be isotropic, the velocity distribution of heavy residues is a symmetric Gaussian[19] of the form

$$\frac{1}{v^2}\frac{d^2\sigma}{d\Omega\,dv}=N\exp(-v_{CN}^2\sin^2\theta/2s^2)\times\exp[-(v-v_{CN}\cos\theta)^2/2s^2]\,, \quad (1)$$

with centroid $\bar{v}=v_{CN}\cos\theta$ and width s, where v and θ are the lab velocity and angle of the heavy residue, respectively, and N is a normalization constant. The width or standard deviation s is a complex function of the evaporation process, depending on the number and type of light particles emitted, and can be calculated using statistical techniques. Whenever possible, the data were converted to a $1/v^2d^2\sigma(d\Omega\,dv)^{-1}$ distribution so that an automatic Gaussian fitting program could be used to determine the experimental areas, centroids, and widths. We consider some examples below which show the presence of additional yields. Subsequently, we discuss what processes could produce these other yields and describe how σ_{fus} was extracted.

Typical velocity distributions $[1/v^2d^2\sigma(d\Omega\,dv)^{-1}]$ for three identified reaction products covering the mass range $A=30$–36 are shown in Fig. 4 for $E_{lab}=180$ MeV, $\theta_{lab}=3°$. These are compared with the evaporation residue velocity distributions generated by the Monte Carlo code PACE.[21] The heavier residues ($A\geq 36$) have a single Gaussian shape given by Eq. (1), and the widths of the generated PACE spectra are in good agreement with experiment. Figure 4(a) is the velocity distribution for ^{36}Cl, typical of the heavier residues which contribute most to the fusion cross section at the extreme forward angles (2°–4°). As no structure in the velocity distributions for residues with $A\geq 36$ other than a symmetric Gaussian was observed, we conclude that these residues are reached purely by single nucleon (xp,yn) emission.

α emission and α mixed with nucleon emission (xp,yn,$z\alpha$) compete with (xp,yn) decay channels for evaporation residues with $A<36$. For these lighter products a definite increase in the complexity of the structure of the velocity spectra is observed, with the result that a single Gaussian no longer properly describes the shapes of the distributions. Figure 4(b) is an example of a probable (2p,n,α) decay to ^{33}S. The velocity spectrum of the residue shows the characteristic double peak due to α particle emission in the forward and backward directions. The centroids of these two peaks are shifted away from $v=v_{CN}\cos\theta$ by the average recoil velocity given to the residue by emission of the α particles. Masses with $A=33$–35 typically have this structure. The widths of calculated distributions for the intermediate masses were generally in agreement with the data; however, in Fig. 4(b) the experimental velocity distribution of ^{33}S extends to slightly higher velocities than the calculation.

Figure 4(c) shows the velocity distribution of ^{30}Si reaction products at $\theta_{lab}=3°$. The calculated distribution is a broad symmetric peak centered at $v=v_{CN}\cos\theta$, corresponding to emission of two α particles and two additional protons (2p,2α). We note that the experimental distribution in Fig. 4(c) has a much greater width than predicted by the statistical code. Yield at residue velocities above

and below those due to successive emission of α particles or nucleons is indicative of the emission of particles with masses in excess of $A=4$. Evaporation residue products observed in the mass range $29 \leq A \leq 32$ have a structure similar to that of ^{30}Si.

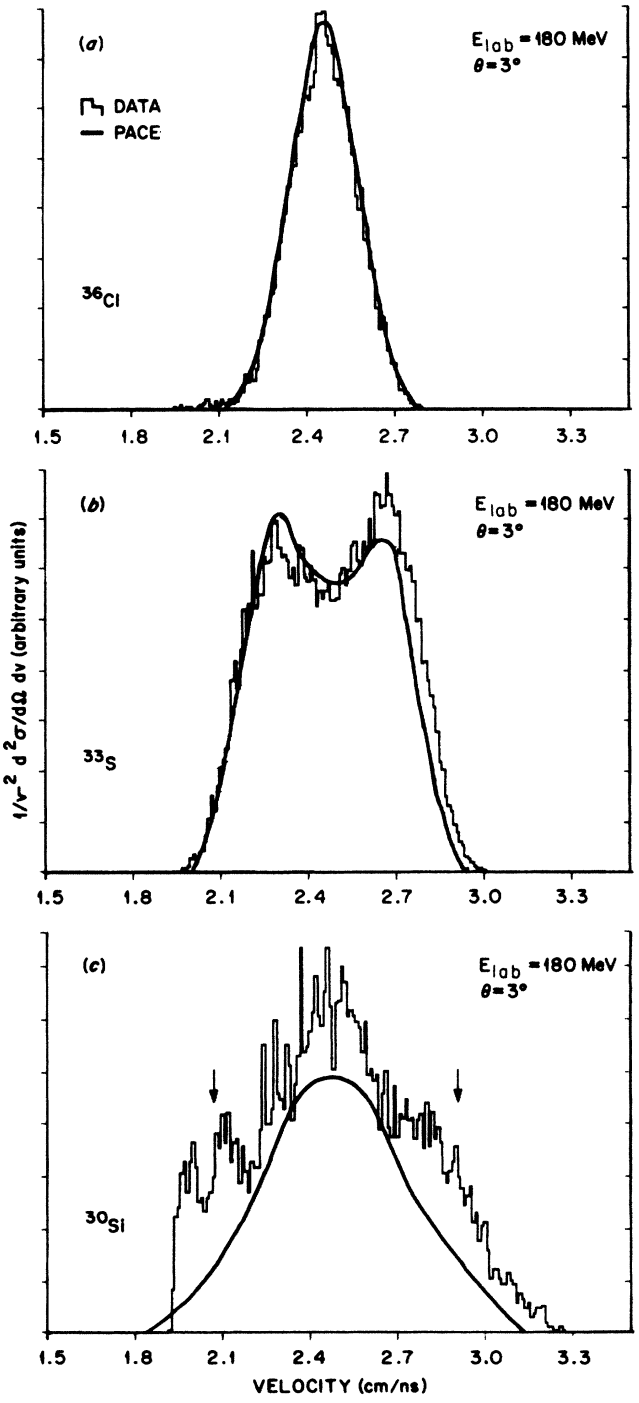

FIG. 4. Velocity distributions for reaction products ^{36}Cl, ^{33}S, and ^{30}Si at $E_{lab}=180$ MeV, $\theta_{lab}=3°$. The histograms are data; the curves show the result of the evaporation calculation with PACE. The two arrows in Fig. 4(c) indicate the locations of centroids for possible yields from the ^{12}C(^{28}Si,^{32}S*)^{8}Be* reaction, with ^{32}S* decaying to ^{30}Si (also see Fig. 5).

Two processes that could contribute to the enhanced width of the velocity distributions such as shown in Fig. 4(c) are (1) a ^{8}Be (or a pair of correlated α particles) may be emitted from the excited compound nucleus, i.e., a decay by (2p,^{8}Be) to ^{30}Si, or (2) some type of deeply inelastic scattering is occurring with mass transfer away from the ^{28}Si + ^{12}C entrance channel, the result being a stable ^{30}Si nucleus. Since Hauser-Feshbach calculations[13,19] generally predict small cross sections ($<5-10\%$ of σ_{fus}) for the emission of massive particles for $A>4$, we consider the latter case, (2). The reaction ^{12}C(^{28}Si,^{8}Be*)^{32}S* is favorable based on the low disassociation energy of ^{12}C into an α particle and a ^{8}Be, with a ground state Q value for ^{12}C(^{28}Si,^{8}Be)^{32}S of -0.43 MeV. The deeply inelastic scattering reaction produces an excited ^{32}S nucleus, which will lose an additional two protons by evaporation to become ^{30}Si. A Monte Carlo calculation was performed to simulate yields from the ^{12}C(^{28}Si,^{8}Be*)^{32}S* reaction. The result is shown in Fig. 5 for $E_{lab}=180$ MeV at $\theta_{lab}=3°$, 6°, and 10°. The calculation represents a situation that would never actually be realized in a real experiment, in a sense that only the ^{32}S* is detected from ^{12}C(^{28}Si,^{8}Be*)^{32}S*. The detector geometry used in the simulation is the same as used in the actual experiment.

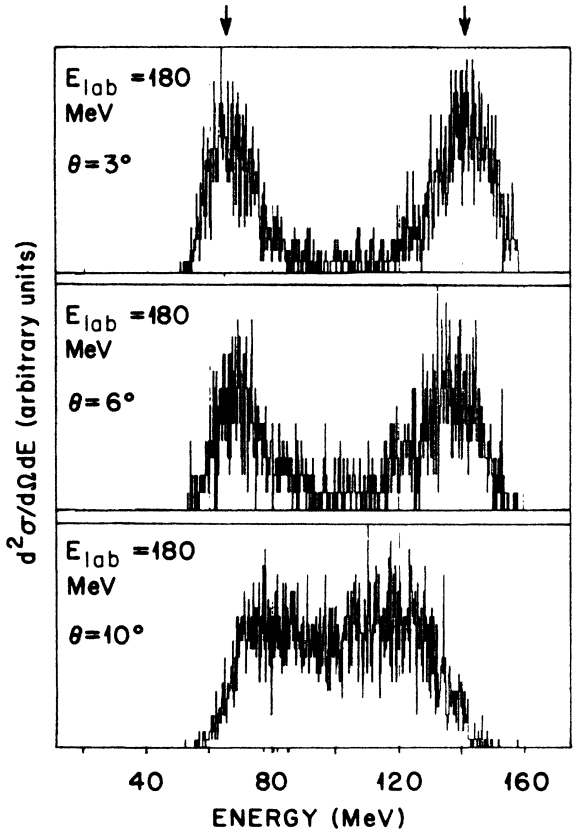

FIG. 5. Simulated energy spectra at 180 MeV, $\theta_{lab}=3°$, 6°, and 10° for the deeply inelastic ^{12}C(^{28}Si,^{32}S*)^{8}Be* reaction (^{32}S* detected). The two arrows in the spectrum at 3° indicating the centroid of the yields correspond to the two velocities shown by arrows in Fig. 4(c).

In the simulation the widths of Q-value distributions measured in deeply inelastic scattering of ^{28}Si on ^{12}C (Refs. 15, 16, and 22) are used to determine a probability for ^{8}Be emission and random trajectories of the outgoing reaction products are generated.[23] The 3° spectrum is shown in Fig. 5 and should be compared to the experimental distribution shown in Fig. 4(c). The arrows indicating the centroids of the low and high velocity (or energy) components of the ^{12}C(^{28}Si,^{8}Be*)^{32}S* in the 3° simulated spectrum of Fig. 5 correspond to the same velocities in the experimental ^{30}Si spectrum of Fig. 4(c). Adjustment for the change in velocity due to the loss of the two protons has been made. Note in Fig. 5 that due to the reaction kinematics, as the laboratory angle increases, the centroids of the low and high velocity components differ less. For angles greater than about 10°, the centroids of yields from such deeply inelastic processes approach the velocity centroid of the compound nucleus residues, making it difficult in the inclusive spectrum to distinguish between contributions from deeply inelastic and compound nuclear reaction processes.

The velocity distributions generated by PACE were compared directly to the data in order to identify any features of the data that did not appear to be evaporation residues of ^{40}Ca*. Assuming that the nonfusion processes produce a heavy fragment which may subsequently decay via light particle emission, the residues of this heavy fragment will have a distribution of velocities around an average value in the form of the Gaussian of Eq. (1). With one or more centroids allowed for a fit, the deconvolution of the compound nucleus residue peaks and other peaks from nonfusion contributions permits the extraction of the fusion cross section. Some interpretation had to be applied in these situations, such as choosing the number of peaks in a spectrum, and determining whether the deconvolution provides a reliable kinematic separation. A check of our procedure could be made by comparing the deconvoluted evaporation residue spectra from the Gaussian fitting procedure with the PACE results. This method provides a way of checking the extraction of the fusion cross section without being solely dependent on the simulation code results for performing the separation. In the example of the ^{30}Si spectrum discussed above [see Fig. 4(c)], the enhanced width of the velocity distribution has been attributed to a deeply inelastic scattering process. The velocities of residues resulting from heavy particle emission ($A > 4$) from the compound nucleus (also sometimes called asymmetric fission) are kinematically similar to the deeply inelastic scattering, and these yields would be excluded from the fusion cross section by the Gaussian fitting procedure. However, we believe this contribution in the mass range $A = 29$–32 amounts to less than the overall uncertainty (6.9%) of the deconvolution.

Figure 6 shows angular distributions (2°–13°) at 180 MeV of all yields from fusion and other processes (solid points), for the same reaction products presented in Figs. 4(a)–4(c). The smooth curves drawn through the data points were used to obtain the integrated isotopic cross sections. Also shown as histograms are the predictions of PACE. The broadening of the angular distribution with decreasing mass due to the emission of more light particles can be seen. For the heavier residues ($A = 34$–37), the calculated angular distributions are in good agreement with the angular distributions derived from integrated velocity spectra, but for lower mass products, $A \gtrsim 33$, the experimental angular distributions appear to extend beyond the maximum angle that is kinematically possible for evaporation residues of the compound nucleus. The evaporation residue yields extracted from the velocity spectra by the procedure described above are represented by the open squares for ^{30}Si in Fig. 6, and it can be seen that the angular distributions of the deconvoluted evaporation residue data are described fairly well by the calculated angular distribution for ^{30}Si evaporation residues.

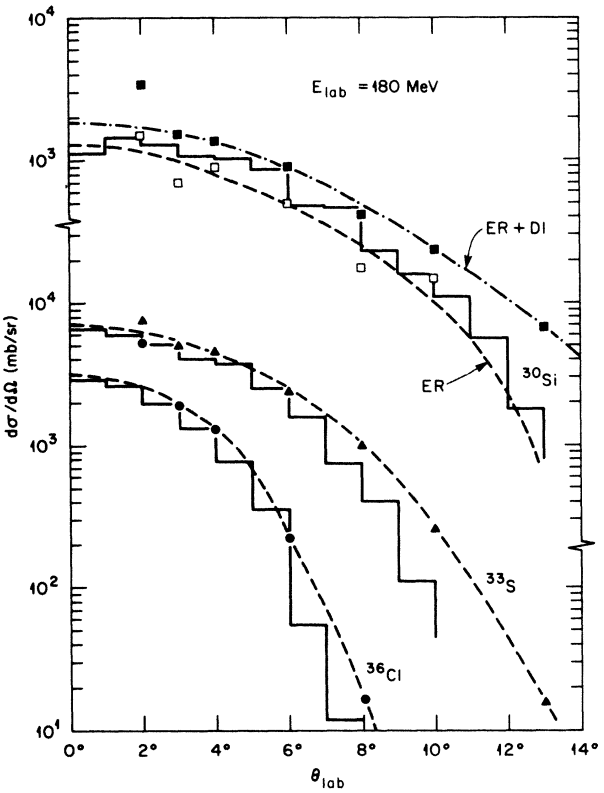

FIG. 6. Angular distributions for ^{30}Si, ^{33}S, and ^{36}Cl at $E_{lab} = 180$ MeV. The solid data points indicate the measured yields from $\theta_{lab} = 2°$–$13°$, and the dashed curves are used for integration of the differential cross sections. The open squares indicate the deconvoluted evaporation residue yields from the Gaussian fitting procedure, with the dotted-dashed curve for integration of the total evaporation residue plus deep inelastic yield. The histograms are the predictions of PACE.

The isotopic cross sections at 130 and 180 MeV lab energies are compared to the evaporation code predictions in Fig. 7. (Experimental results are also listed in Table I.) The extended crosses shown for some isotopes, particularly the lighter ones, indicate the amount of nonfusion yield extracted in the analysis. The yields indicated by the extended crosses which point up were not included in the summation of the fusion cross section. Overall, the calculation was accurate in predicting the centroid of the mass

distribution; however, it shows a tendency to become less reliable as more light particles are emitted. Changes in the yrast line, entry spin, or addition of discrete levels have the most effect on the magnitude of isotopic cross sections for residues reached by $(x\text{p},y\text{n},2\alpha)$ and $(x\text{p},y\text{n},3\alpha)$ decays. The calculation shown in Fig. 7 uses options of the code which are considered the defaults, which are the diffuse-surface yrast line of Sierk,[24] the level density parameter a = mass/7.5, and the Gilbert-Cameron level density formulas.[25] No discrete levels have been added.

Summing the isotopic yields, we find the cross sections at 130 and 180 MeV lab energies. At 145 and 160 MeV, the cross sections were obtained by linear interpolation of the slowly varying function $\sigma = f(d\sigma/d\Omega(3°)\sigma^{-1})$. Table II lists cross sections and the maximum angular momentum for fusion extracted with the sharp cutoff approximation. The uncertainty in the cross sections consists of the experimental error, 11% (see Sec. II), uncertainties in correcting for low energy cutoff in the experimental spectra [5.9% at 130 MeV and $<0.5\%$ at 180 MeV; see, for example, Fig. 4(c)], 6.9% uncertainty due to the procedure used for separating damped yields at 180 MeV, 3.0% for the same at 130 MeV, 3.0% for extrapolating beyond 2° (negligible beyond 13°), and the missing cross section for evaporation residues with masses equal or lighter than that of the projectile mass, 1.0%. These contributions combine for an overall uncertainty at all energies of 13%. The remainder of the yield σ_{nf} (all nonfusion yields) from 2° to 13° shows what was excluded from σ_{fus}. The quoted σ_{nf} represents only the yield which is present in the forward cone covered in this experiment ($\theta_{lab} \leq 13°$) for $Z \geq 12$ and $A \geq 24$; it should not be considered, when added to σ_{fus}, as a measure of the total reaction cross section.

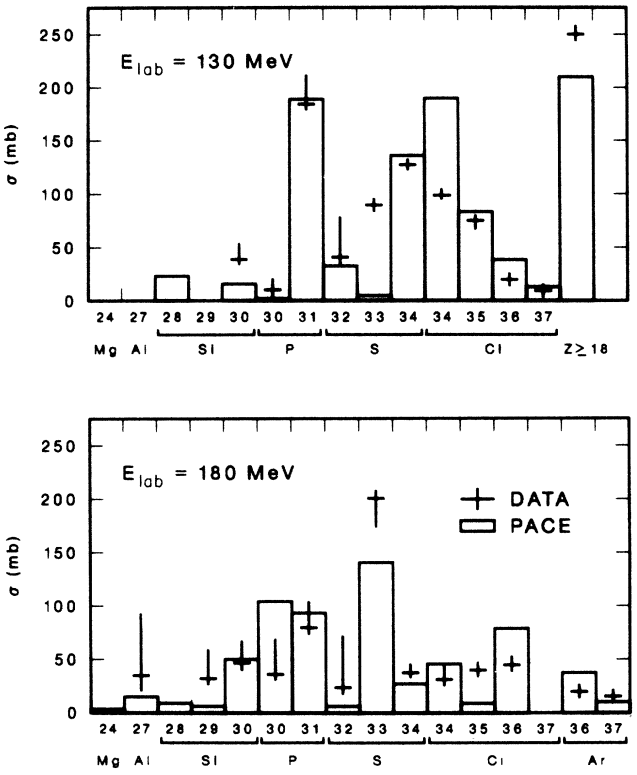

FIG. 7. Integrated isotopic yields for evaporation residues identified by charge and mass. Extended crosses above indicate the presence of nonfusion yields excluded from σ_{fus}. The bars are the result of PACE calculations with the input specified in the text.

TABLE I. Partial cross sections for identified reaction products.

	$E_{lab}=130$ MeV			$E_{lab}=180$ MeV	
	σ_{fus} (mb)	σ_{nf}[a] (mb)		σ_{fus} (mb)	σ_{nf}[a] (mb)
$Z \geq 18$	254		^{37}Ar	18	
^{37}Cl	11		^{36}Ar	21	
^{36}Cl	22		^{36}Cl	48	
^{35}Cl	74		^{35}Cl	43	
^{34}Cl	100		^{34}Cl	32	
^{35}S	2		^{35}S	6	
^{34}S	128		^{34}S	40	
^{33}S	91		^{33}S	203	
^{32}S	40	42	^{32}S	24	50
^{32}P	13		^{33}P	5	
^{31}P	186	34	^{32}P	14	2
^{30}P	9	10	^{31}P	86	19
^{30}Si	40	13	^{30}P	36	39
^{28}Si	23[b]		^{29}P	13	
			^{30}Si	46	23
			^{29}Si	34	24
			^{28}Si	20[b]	
			^{27}Al	35	58
			^{24}Mg	≤ 5	

[a] σ_{nf} represents yield excluded from σ_{fus}.

[b] Estimated evaporation residue cross section at the projectile mass.

TABLE II. Evaporation residue cross sections.

E_{lab} (MeV)	$E_{c.m.}$ (MeV)	σ_{fus} (mb)	l_{cr} ($\hbar$)	σ_{nf} (mb)
130	39	992±64	21.7±0.8	98±15
145	43.5	893±58[a]	21.8±0.7	
160	48	844±55[a]	22.2±0.8	
180	54	728±48	21.9±0.8	214±25

[a]Obtained by interpolation from the measured $d\sigma/d\Omega$ at 3° and σ_{fus} at 130 and 180 MeV.

IV. DISCUSSION

Figure 8(a) shows ^{28}Si + ^{12}C evaporation residue data from a number of experiments in the low to intermediate energy regions: Lesko *et al.*,[26] Gary and Volant,[27] and Hugi *et al.*,[28] and the cross sections obtained at $E_{c.m.}$ = 39–54 MeV in the present measurement. To illustrate how the measured evaporation residue cross sections can be related to the observed behavior of deeply inelastic scattering in the ^{28}Si + ^{12}C system,[16] we also present several fusion model calculations in Fig. 8(a). Curves 1 and 2 are the predicted excitation functions of Bass[12,13] and curve 3 is the classical trajectory model of Birkelund *et al.*[14] The empirical nuclear potential of Bass is specified by the function $g(x)$,[13]

$$g(x)=\frac{1}{Ae^{x/a}+Be^{x/b}} \quad \text{with } V_{nuc}(d)=\frac{R_1R_2}{R_1+R_2}g(x)\ , \tag{2}$$

where $d=R_1+R_2+x$ is the distance from center to center of the two nuclei, and A, a, B, and b are parameters. The parametrization from Ref. 12, A = 0.03 MeV^{-1} fm, a = 3.30 fm, B = 0.0061 MeV^{-1} fm, and b = 0.65 fm, which is based on a global fit to fusion data, was used in the calculation of curve 1. The second Bass calculation (curve 2) reflects a different parametrization of the nuclear potential that yields the observed kinetic energies of scattered fragments in the experiment of Ref. 16. It was found that the total kinetic energy of the outgoing fragments as a function of the center of mass bombarding energy increased linearly to $E_{c.m.}$ ~45 MeV, then remained constant for all higher energies measured. The interpretation of this behavior[16] lead to extraction of a critical angular momentum for the orbiting dinuclear system l_{cr}^{orb}, obtained by using the Bass potential to calculate the kinetic energy of the fragments and adjusting the above parameters to produce the observed energy E_{kin} at the center of mass energy $E_{c.m.}$ where the saturation occurs.

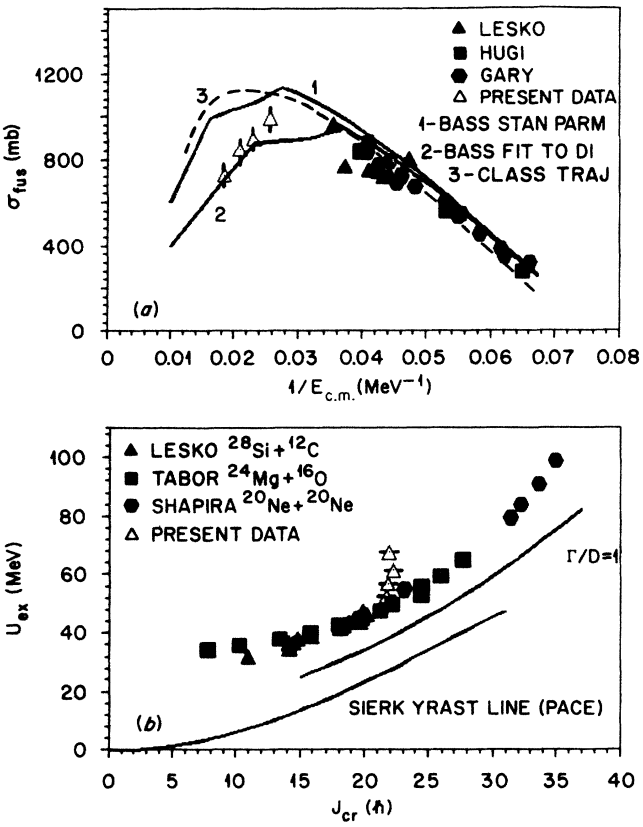

FIG. 8. (a) Fusion cross sections for ^{28}Si + ^{12}C from Refs. 26–28. The solid lines are calculated excitation functions of the Bass (Ref. 12) and classical trajectory (Ref. 14) models (see text). (b) Extracted J_{cr} from fusion data where the same compound nucleus ^{40}Ca was formed by way of entrance channels ^{28}Si + ^{12}C (Ref. 26), ^{24}Mg + ^{16}O (Ref. 33), and ^{20}Ne + ^{20}Ne (Ref. 34). Also shown are the yrast line from PACE and the Γ/D_J criterion of Vandenbosch (Ref. 11).

Table III shows the parameters used for each curve in Fig. 8(a), as well as the E_{kin}, $E_{c.m.}$, and extracted l_{cr}^{orb} and l_{cr}^{fus}(Bass), where all quantities quoted are understood to be at the saturation point. l_{cr}^{orb} represents the critical angular momentum of the exit channel. It is related to the critical angular momentum in the entrance channel which fuses l_{cr}^{fus}(Bass) by the friction form factor f as $l_{cr}^{orb}=fl_{cr}^{fus}$(Bass), where f accounts for the reduction of angular momentum due to the damping process during the collision. The factor f is usually defined to be $J_{12}/(J_{12}+J_1+J_2)$ for sticking friction or $\frac{5}{7}$ for rolling friction in the Bass model.[13] The original set of parameters produces not only the overestimation of the fusion cross section at high energy, but also it can be seen from the table that the saturation energy $E_{c.m.}$ is also over 20 MeV higher than measured. Changing only the strength parameter A produces reasonable agreement with the experimental fusion cross section and also reproduces the critical behavior of the observed damped scattering ($E_{c.m.}$ = 45 MeV, E_{kin} = 24 MeV)

TABLE III. Fusion model calculations. Curves 1 and 2, Bass model; curve 3, classical trajectory model.

Curve	A (MeV^{-1} fm)	a (fm)	B (MeV^{-1} fm)	b (fm)	$E_{c.m.}$ (MeV)	E_{kin} (MeV)	l_{cr}^{orb} ($\hbar$)	l_{cr}^{fus}(calc) ($\hbar$)
1	0.030	3.30	0.0061	0.65	67.3	37.2	24	29
2	0.045	3.30	0.0061	0.65	47.1	27.7	19	23
3	Blocki potential				69.0	36.6	22	29

within 4 MeV for E_{kin}. Generally, the use of sticking friction gave a better fit to the data than did the use of weaker rolling friction. For $E_{kin}=24$ MeV the center of mass energy for saturation is somewhat lower, near 40 MeV, and the corresponding l_{cr}^{orb} and l_{cr}^{fus}(Bass) also decrease.

For comparison to the above results, a classical trajectory calculation[14] is also presented (curve 3) with the Bondorf Coulomb potential,[29] the nuclear proximity potential of Blocki,[30] and the proximity friction of Randrup.[31] The friction is applied from the barrier radius inward, instead of at one point ($R_{cr}=R_1+R_2$) as in the Bass model; hence the excitation function has no abrupt changes in slope.

The lower energy behavior of curves 1–3 (region I as discussed with regard to Fig. 1) are very similar and are in agreement with the data up to the energy region (regions II and III) where friction effects are important in determining the magnitude of the cross section. Those partial waves in the entrance channel which fuse due to the presence of friction now appear approximately $6\hbar$ lower [for l_{cr}^{fus}(calc)] for curve 2 than curves 1 and 3. Curve 3 differs by $\sim 10\%$ at lower energy from the Bass calculations, due, for the most part, to the difference in the empirical and the theoretical nuclear potentials,[32] but is comparable to the Bass curve 1 at high energy [l_{cr}^{fus}(clas traj) $=29\hbar$].

A plot of excitation energy as a function of the l_{cr} for fusion is shown in Fig. 8(b) for data obtained by Lesko *et al.*,[26] Tabor *et al.*,[33] and Shapira *et al.*[34] along with the present data for different entrance channels that populate the same compound nucleus ^{40}Ca. The yrast line used in the statistical evaporation code[24] for calculations in the present work and the Γ/D_J criterion of Vandenbosch and Lazzarini[11] are also shown. The difference in the entrance channels defined by the grazing angular momentum can be seen in the ^{24}Mg + ^{16}O and ^{28}Si + ^{12}C channels at excitations of 33–45 MeV. Lesko *et al.*[26] have already noted that at $E^* \sim 45$ MeV the two data sets appear to approach each other; in fact, the ^{20}Ne + ^{20}Ne data suggest a continuity extending to higher E^*. The high energy ^{28}Si + ^{12}C data are in contrast with this trend. These data show a clear entrance channel limit imposed on the fusing system where we reach an l_{cr}^{fus} of $22\hbar$ at high excitation energy.

V. SUMMARY

We have presented evaporation residue data for the ^{28}Si + ^{12}C system for bombarding energies of 4.6–6.4 MeV/nucleon. Unit mass and charge identification of the reaction products and a careful kinematic analysis, assisted by Monte Carlo simulation codes for compound nucleus decay and deeply inelastic scattering, allowed us to separate compound nucleus residues from yields due to nonfusion processes. We have determined that the fusion of ^{28}Si + ^{12}C at these higher energies is limited by the entrance channel rather than by compound nucleus constraints. The existence of data on orbiting for the same system, which show a saturation of the fragments' kinetic energy as a function of bombarding energy, lead to the extraction of a critical angular momentum limiting capture in this system (l_{cr}^{orb}). The resulting value of l_{cr}^{fus}(Bass) is in reasonable agreement with the experimental l_{cr} for fusion of ^{28}Si with ^{12}C, supporting the idea that the system forms a long-lived dinuclear complex prior to compound nucleus formation.[35]

Further measurements are planned to investigate the fusion excitation function in similar light-heavy ion systems and for ^{28}Si and ^{12}C up to 9 MeV/nucleon. Of interest are the contributions of incomplete fusion to the total reaction cross section. A quantitative study of the onset and behavior of incomplete fusion and its competition with fusion may be possible. More detailed calculations are also underway[36] that should further elucidate the connection between the fusion and orbiting processes.

ACKNOWLEDGMENTS

The authors wish to thank J. Beene for assistance with PACE calculations and C. Glover for use of his graphics software program. Oak Ridge National Laboratory is operated by Martin Marietta Energy Systems, Inc. under Contract No. DE-AC05-840R21400 with the U.S. Department of Energy.

[1]D. Horn, A. J. Ferguson, and O. Häusser, Nucl. Phys. **A311**, 238 (1978).

[2]J. P. Wieleczko, S. Harar, M. Conjeaud, and F. Saint-Laurent, Phys. Lett. **93B**, 35 (1980).

[3]F. Saint-Laurent, M. Conjeaud, S. Harar, J. M. Loiseaux, J. Menet, and J. B. Viano, Nucl. Phys. **A327**, 517 (1979).

[4]D. E. DiGregorio, J. Gomez del Campo, Y. D. Chan, J. L. C. Ford, Jr., D. Shapira, and M. E. Ortiz, Phys. Rev. C **26**, 1490 (1982).

[5]J. F. Mateja, A. D. Frawley, D. G. Kovar, D. Henderson, H.

Kiezoe, R. V. F. Janssens, G. Rosner, G. S. F. Stephans, B. Wilkins, R. T. Lesko, and M. F. Vineyard, Phys. Rev. C **31**, 867 (1985).

[6]J. Gomez del Campo, J. A. Biggerstaff, R. A. Dayras, D. Shapira, A. H. Snell, P. H. Stelson, and R. G. Stokstad, Phys. Rev. C **29**, 1722 (1984).

[7]D. G. Kovar, D. F. Gessaman, T. H. Braid, Y. Eisen, W. Henning, T. R. Ophel, M. Paul, K. E. Rehm, S. J. Sanders, P. Sperr, J. P. Schiffer, S. L. Tabor, S. Vigdor, and B. Zeidman, Phys. Rev. C **20**, 1305 (1979).

[8]D. Glas and U. Mosel, Nucl. Phys. **A237**, 429 (1975).

[9]M. Diebel, D. Glas, U. Mosel, and H. Chandra, Nucl. Phys. **A333**, 253 (1980).

[10]S. M. Lee, T. Matsuse, and A. Arima, Phys. Rev. Lett. **45**, 165 (1980).

[11]R. Vandenbosch and A. J. Lazzarini, Phys. Rev. C **23**, 1074 (1981).

[12]R. Bass, Phys. Rev. Lett. **39**, 265 (1977).

[13]R. Bass, *Nuclear Reactions with Heavy Ions* (Springer-Verlag, New York, 1980), pp. 267 and 318–369.

[14]J. R. Birkelund, L. E. Tubbs, and J. R. Huizenga, Phys. Rep. **56**, 107 (1979).

[15]D. Shapira, R. Novotny, Y. D. Chan, K. A. Erb, J. L. C. Ford, Jr., J. C. Peng, and J. D. Moses, Phys. Lett. **114B**, 111 (1982).

[16]D. Shapira, D. Schull, J. L. C. Ford, Jr., B. Shivakumar, R. L. Parks, R. A. Cecil, and S. T. Thornton, Phys. Rev. Lett. **53**, 1634 (1984).

[17]A. Breskin, Nucl. Instrum. Methods **196**, 11 (1982).

[18]J. L. Blankenship, F. E. Obenshain, and A. H. Snell, in Oak Ridge National Laboratory Report No. ORNL-6120, edited by A. B. Livingston, 1985.

[19]J. Gomez del Campo, R. G. Stokstad, J. A. Biggerstaff, R. A. Dayras, A. H. Snell, and P. H. Stelson, Phys. Rev. C **19**, 2170 (1979).

[20]L. C. Northcliffe and R. F. Schilling, Nucl. Data A **7**, 233 (1970).

[21]A. Gavron, Phys. Rev. C **21**, 230 (1980).

[22]D. Shapira, J. Gomez del Campo, J. L. C. Ford, Jr., B. Shivakumar, P. H. Stelson, B. A. Harmon, R. L. Parks, and S. T. Thornton, Nucl. Instrum. Methods B **10/11**, 436 (1985).

[23]R. Novotny, D. Shapira, and S. T. Thornton (unpublished).

[24]The compound nucleus statistical decay program PACE has a modified liquid drop model calculation in the code for the yrast line written by A. J. Sierk.

[25]A. Gilbert and A. G. W. Cameron, Can. J. Phys. **43**, 1446 (1965).

[26]K. T. Lesko, D.-K. Lock, A. Lazzarini, R. Vandenbosch, V. Metag, and H. Doubre, Phys. Rev. C **25**, 872 (1982).

[27]S. Gary and C. Volant, Phys. Rev. C **25**, 1877 (1982).

[28]M. Hugi, J. Lang, R. Müller, E. Ungricht, K. Bodek, L. Jarczyk, B. Ramys, A. Magiera, A. Strzalkowski, and G. Willim, Nucl. Phys. **A368**, 173 (1981).

[29]J. P. Bondorf, J. R. Huizenga, M. I. Sobel, and D. Sperber, Phys. Rev. C **11**, 1265 (1975).

[30]J. Blocki, J. Randrup, W. J. Swiatecki, and C. F. Tsang, Ann. Phys. (Leipzig) **105**, 427 (1977).

[31]J. Randrup, Ann. Phys. (Leipzig) **112**, 356 (1978).

[32]R. Bass, in *Fusion and Deep Inelastic Reactions,* Vol. 117 of *Lecture Notes in Physics,* edited by W. von Oertzen (Springer-Verlag, Berlin, 1979), p. 287.

[33]S. L Tabor, D. F. Geesaman, W. Henning, D. G. Kovar, and K. R. Rehm, Phys. Rev. C **17**, 2136 (1978).

[34]D. Shapira, D. DiGregorio, J. Gomez del Campo, R. A. Dayras, J. L. C. Ford, Jr., A. H. Snell, P. H. Stelson, R. G. Stokstad, and F. Pougheon, Phys. Rev. C **28**, 1148 (1983).

[35]M. A. Hussein, B. V. Carlson, O. Civitarese, and A. Szanto De Toledo, Phys. Rev. Lett. **54**, 2659 (1985).

[36]B. Shivakumar, S. Ayik, B. A. Harmon, and D. Shapira, submitted to Phys. Rev. Lett.